Acta Materialia 126 (2017) 132–144

Contents lists available at ScienceDirect

Acta Materialia

journal homepage: www.elsevier.com/locate/actamat

Full length article

Twin recrystallization mechanisms and exceptional contribution to texture evolution during annealing in a magnesium alloy

Dikai Guan, W. Mark Rainforth*, Le Ma, Brad Wynne, Junheng Gao

Department of Materials Science and Engineering, The University of Sheffield, Sheffield, S1 3JD, UK

ARTICLE INFO

Article history:
Received 15 November 2016
Received in revised form
20 December 2016
Accepted 22 December 2016
Available online 30 December 2016

Keywords:
Magnesium alloy
Recrystallization
Deformation twin
Texture evolution

ABSTRACT

The formability and mechanical properties of Mg alloys are strongly related to the crystallographic basal texture. Deformation twins form extensively after mechanical processing. Recrystallized grains originating from twins usually randomize the texture and therefore weaken the strong deformed texture. It is crucial to understand different recrystallization mechanisms as a function of twin type and therefore their corresponding contribution to texture modification. This work shows that the recrystallization volume fraction formed within twins has been completely underestimated. Specifically, recrystallized grains originating from double twins make the main contribution to texture modification, which contrasts to the opposite view that has been reported in the past decades. The preferential nucleation site, subsequent grain growth and evolution of recrystallization texture in double twins has been tracked in individual twins through the whole annealing process for the first time. After annealing for 378 min at 490 °C, the volume fraction of total recrystallization was ~75.7%, while the recrystallized volume fraction originating from double twins and double twin-grain boundary intersections was ~52.9%, which represents ~69.9% of the total volume fraction recrystallization. Recrystallization mechanisms related to various twin types, twin variants, twin-twin and twin-grain boundaries intersections are precisely determined. These findings could lead new insight to design new wrought alloys and improve formability of commercial alloys.

1. Introduction

The detrimental anisotropic mechanical properties of wrought Mg alloys can be reduced by weakening the basal crystallographic texture [1–4]. Recrystallization leading to the reduction in basal texture intensity has been the focus of considerable attention in the processing of current Mg alloys and the design new wrought Mg alloys with good formability [5–9].

In deformed Mg alloys, four proposed nucleation sites for recrystallization are grain boundaries, shear bands, deformation twins and second phase particles [8,10–12]. Recrystallization grains at the latter three sites have random orientations and potentially weaken the basal texture [11,13–15]. The recrystallization texture also depends on subsequent grain growth of the recrystallized grains [10,12,16–18]. Because of insufficient active slip systems, twinning always occurs and is an important deformation mode at room temperature in Mg alloys [19–27]. The exact correlation of recrystallization evolution with twin types and the effect this has on texture evolution has not been systematically studied.

The recrystallization nucleation sites within twins, at twin–twin or twin–grain boundary (GB) intersections have been extensively reported [13,28–30]. Recrystallization within $\{10\bar{1}2\}$ tension twins (TTWs) rarely occurs since the matrix within these twins is usually unfavourably oriented for basal slip [5,12,22]. In contrast, recrystallization within $\{10\bar{1}1\}$ compression twins (CTWs) and $\{10\bar{1}1\}$-$\{10\bar{1}2\}$ double twins (DTWs) is often observed as a result of basal slip occurring within the twins. This results in a build up in the internal stored energy, since the dislocations cannot penetrate the twin boundaries and facilitates subsequent recrystallization and growth [9,12,18,28,31,32]. Nevertheless, the recrystallized grains within CTWs and DTWs generally cannot grow beyond twin boundaries, and so they make a limited contribution to final texture modification of the overall material [5,6,28,32,33]. Recently, it has been reported that recrystallized grains originating from DTW twin-twin and twin–GB intersections can expand into surrounding deformed parent grains [13,22,28–30,34]. However, systematic work has not been undertaken to understand how this contributes

* Corresponding author.
E-mail address: m.rainforth@sheffield.ac.uk (W.M. Rainforth).

http://dx.doi.org/10.1016/j.actamat.2016.12.058

Table 1
Chemical composition of as-received WE43 alloy.

	Fe	HR	Li	Mn	Nd	Tr	Y	Zn	Zr	To	Mg
wt%	0.002	0.69	<0.005	0.01	2.2	2.9	3.9	<0.005	0.46	<0.01	Balance

to the final texture. This is surprising given that twin recrystallization is the dominant recrystallization process, and therefore is critical to texture evolution in Mg alloys.

Most current observations in the literature have been determined by examining a single point during partial recrystallization or investigating the structure after full recrystallization. In both cases, the evolution of the recrystallization with annealing time is not known. Thus, there are many unanswered questions about the recrystallization process. For example, because both CTWs and DTWs are narrow, what happens when small recrystallized grains, constrained by the twin boundaries, meet adjacent larger recrystallization grains originating from other nucleation sites? It is known that TTWs with low Schmid Factors do not recrystallize, but not known whether TTWs with high Schmid Factors or other reported tension twin variants recrystallize [35]?

In this work we examined the recrystallization process during isothermal annealing of a cold-rolled commercial alloy WE43. We successfully employed a *quasi-in-situ* electron backscatter diffraction (EBSD) method to allow a site-specific method to follow the recrystallization process at each point in the microstructure and therefore to follow the evolution of recrystallization of each twin type. The evolution of the recrystallization process was correlated to twin type, twin variant, the presence of a mixture of different twin types, and at twin-twin and twin-GB intersections within individual deformed parent grains. As a result of these sequential observations, the various twin recrystallization mechanisms are precisely identified. It is shown that twin recrystallization is the main component of recrystallized texture rather than what has hitherto been believed to be a limited contribution. Understanding the twin evolution in detail should be an aspect in the design of new wrought Mg alloys and for optimizing the thermomechanical processes to improve formability of commercial Mg alloys.

2. Experimental procedure

A commercial WE43 alloy supplied by Magnesium Elektron as-extruded T5 bar was used in this work, of composition given in Table 1. A rectangular plate 50 (ED) × 25 (TD) × 6 (ND) mm^3 was cut from the extruded bar (where ED is the extrusion direction, TD the transverse direction and ND the normal direction) for heat treatment and cold rolling.

Solid solution treatment was carried out in a tube furnace with continuous argon flow at 525 °C for 24 h, followed by cold water quenching. The heat treated sample was then cold rolled with a reduction of 20% in one pass. The cold-rolled sample was ground and polished using SiC paper, 1 μm, 0.25 μm diamond suspension, 40 nm OPS suspension. Before putting the sample into a scanning

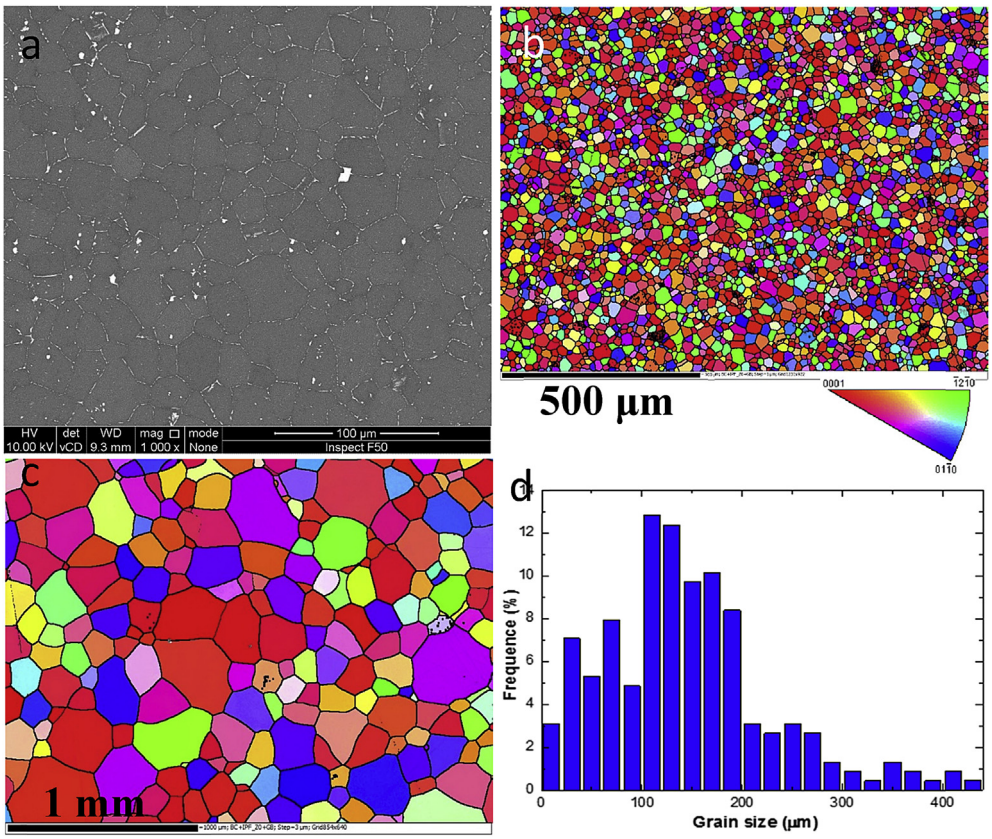

Fig. 1. (a) Backscattered SEM image, (b) EBSD IPF image of as-received WE43 sample. (c) EBSD IPF map and (d) corresponding grain size distribution of 24 h solid solution treated sample. The extrusion direction is horizontal.

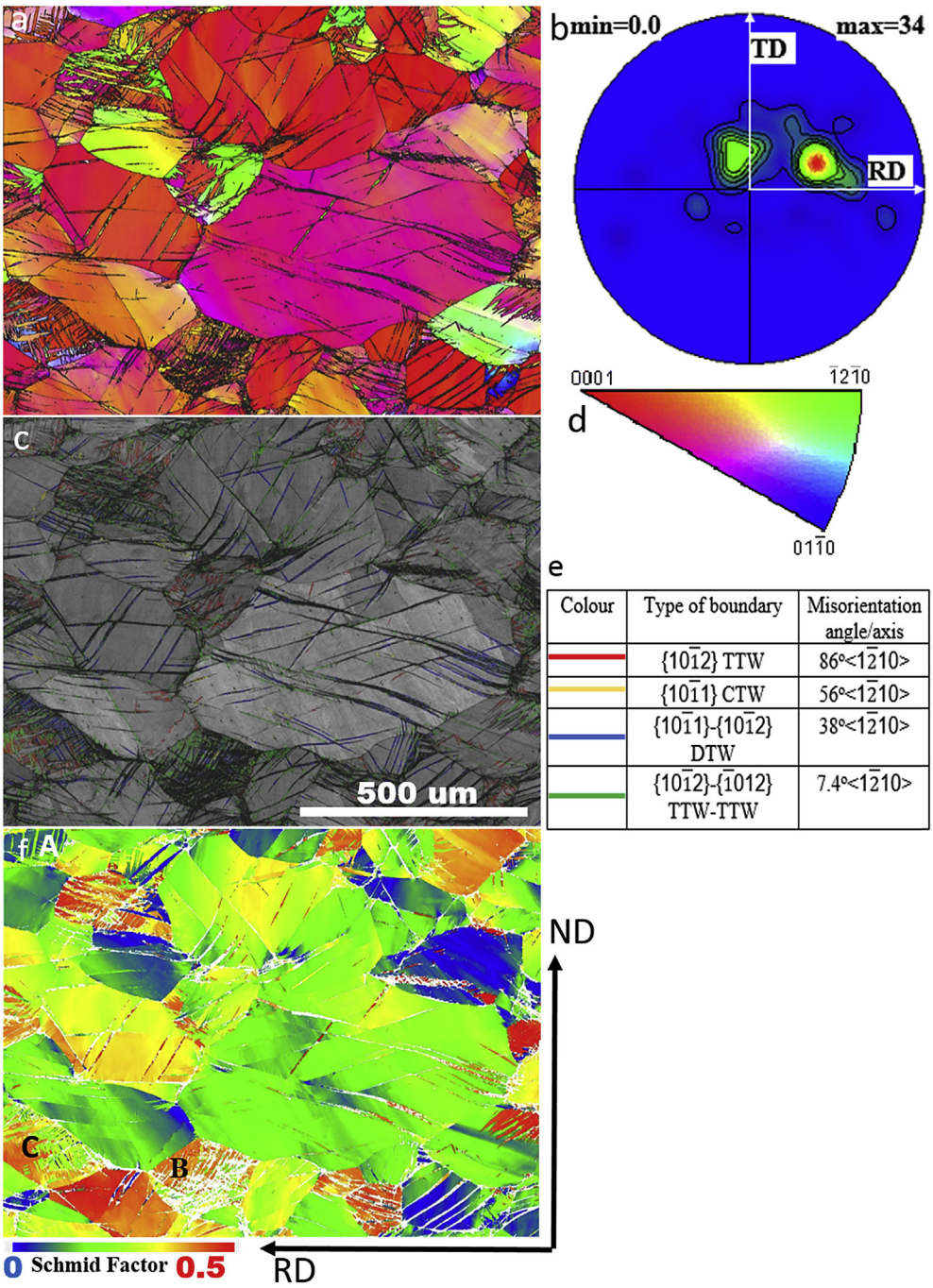

Colour	Type of boundary	Misorientation angle/axis
	$\{10\bar{1}2\}$ TTW	86°<$1\bar{2}10$>
	$\{10\bar{1}1\}$ CTW	56°<$1\bar{2}10$>
	$\{10\bar{1}1\}$-$\{10\bar{1}2\}$ DTW	38°<$1\bar{2}10$>
	$\{10\bar{1}2\}$-$\{\bar{1}012\}$ TTW-TTW	7.4°<$1\bar{2}10$>

Fig. 2. (a) EBSD IPF maps superimposed by band contrast (BC) and (d) corresponding legend of IPF map, (b) (0002) pole figure, (c) BC map superimposed by various twin boundaries, (e) the most common twin types in the cold-rolled sample, and (f) basal Schmid Factor map.

electron microscope (SEM), a Gatan precision etching and coating system (PECS) was employed for final polishing.

Electron Backscatter Diffraction (EBSD) was performed using a FEI Sirion field emission gun SEM fitted with Oxford Instruments HKL Nordlys F EBSD detector. The EBSD scan step size for cold-rolled sample was 0.4 μm, while for annealed samples was around 0.8 μm. The EBSD data were analysed via using HKL CHANNEL5 software, which offers essential tools to process the data. Fiducial marks were made on the surface of the cold-rolled sample after OPS polishing. Thus the area scanned for EBSD was precisely relocated after further annealing to allow re-scanning of exactly the same area. The *quasi-in-situ* EBSD collected data

Table 2
Misorientations between the matrix and primary or secondary twins commonly observed in Mg.

Type of twin	Misorientation angle/axis
$\{10\bar{1}1\}$	56°⟨$1\bar{2}10$⟩
$\{10\bar{1}2\}$	86°⟨$1\bar{2}10$⟩
$\{10\bar{1}3\}$	64°⟨$1\bar{2}10$⟩
$\{10\bar{1}1\}$–$\{10\bar{1}2\}$	38°⟨$1\bar{2}10$⟩
$\{10\bar{1}3\}$–$\{10\bar{1}2\}$	22°⟨$1\bar{2}10$⟩

Table 3
Misorientations generated between different {10$\bar{1}$2} twin variants.

Type of twin	Misorientation angle/axis
{10$\bar{1}$2}-{$\bar{1}$012}	7.4°⟨1$\bar{2}$10⟩
{10$\bar{1}$2}–{01$\bar{1}$2}	60.0°⟨10$\bar{1}$0⟩[a]
{10$\bar{1}$2}–{0$\bar{1}$12}	60.4°⟨8$\bar{1}$ $\bar{7}$0⟩[b]

[a] Actual axis is 3.7° off ⟨10$\bar{1}$0⟩.
[b] Actual axis is 0.2° off ⟨8$\bar{1}$ $\bar{7}$0⟩.

from a large area of about 1.1 mm^2 from the middle part of ND-RD plane. Afterwards, the EBSD scans were taken after 5, 11, 18.5, 28.5, 58, 98, 198 and 378 min annealing at 490 °C. After every EBSD run, the sample was transferred into an argon glove box and sealed in a small aluminium vial. Subsequent annealing was undertaken in a tube furnace with flowing argon with the sample contained in the vial for protection. After annealing, water quenching was undertaken, with the vial providing protection from the water, such that the region of interest on the surface of

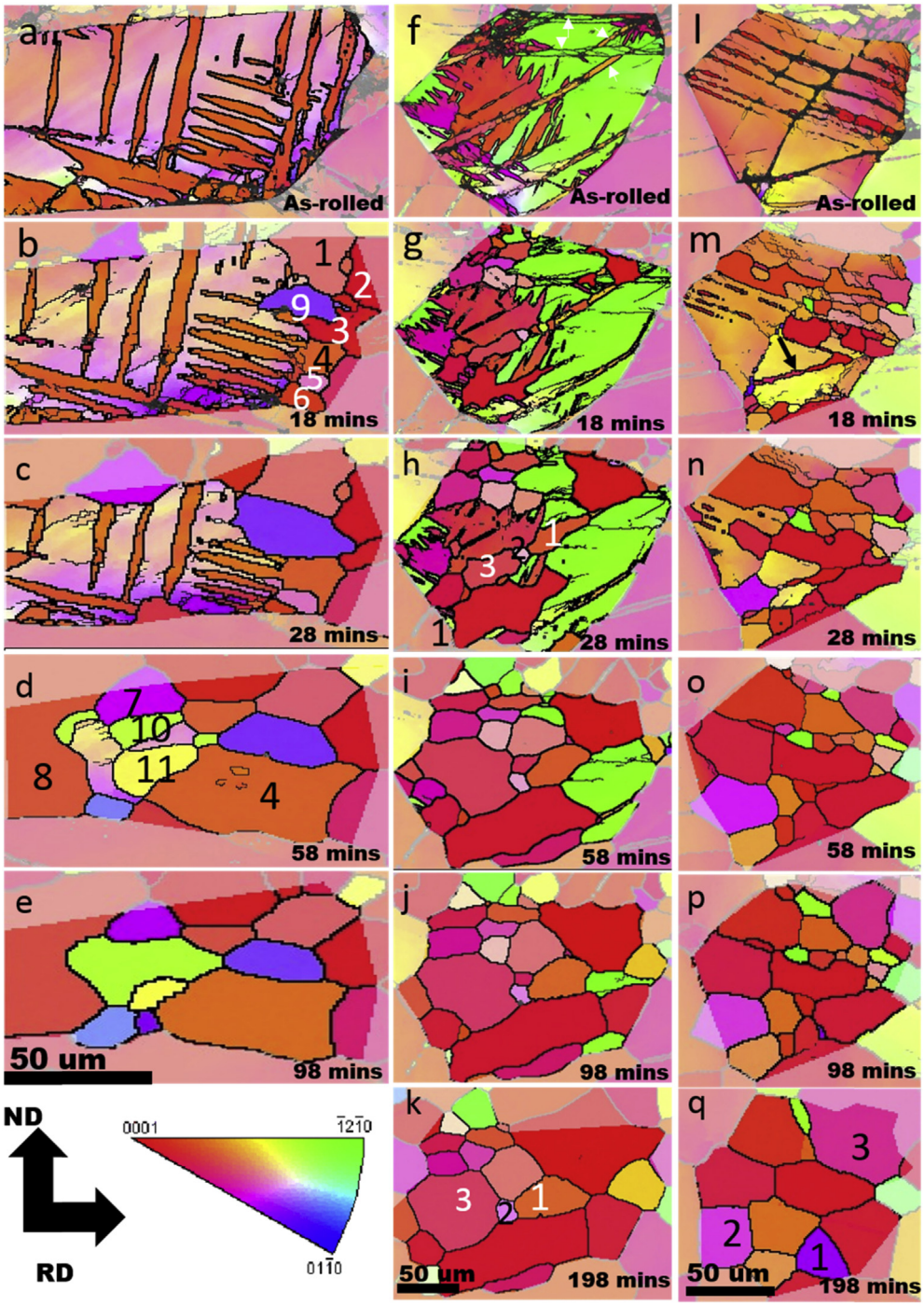

Fig. 3. *Quasi-in-situ* EBSD IPF maps superimposed by band contrast displaying evolution of twins in individual grains annealed at 490 °C with various times (a–e) TTW, (f–k) Primary TTW, TTW-TTW, secondary DTW and (l–q) DTW network.

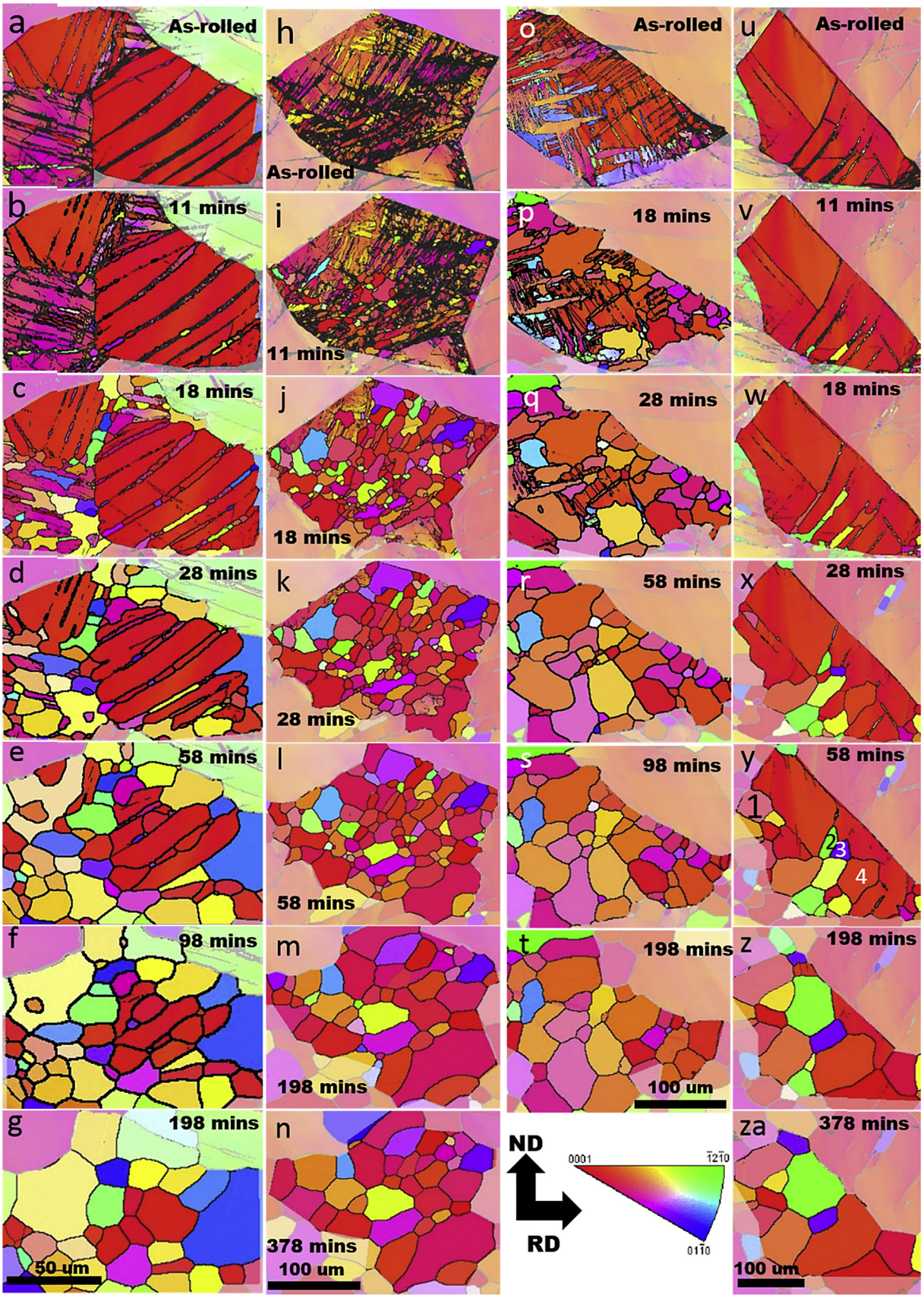

Fig. 4. *Quasi-in-situ* EBSD IPF maps superimposed by band contrast maps displaying evolution of twins in individual grains annealed at 490 °C with various times (a–g) DTW, (h–n) DTW, TTW-TTW, (o–t) DTW, TTW, TTW-TTW and (u-za) DTW-GB intersections.

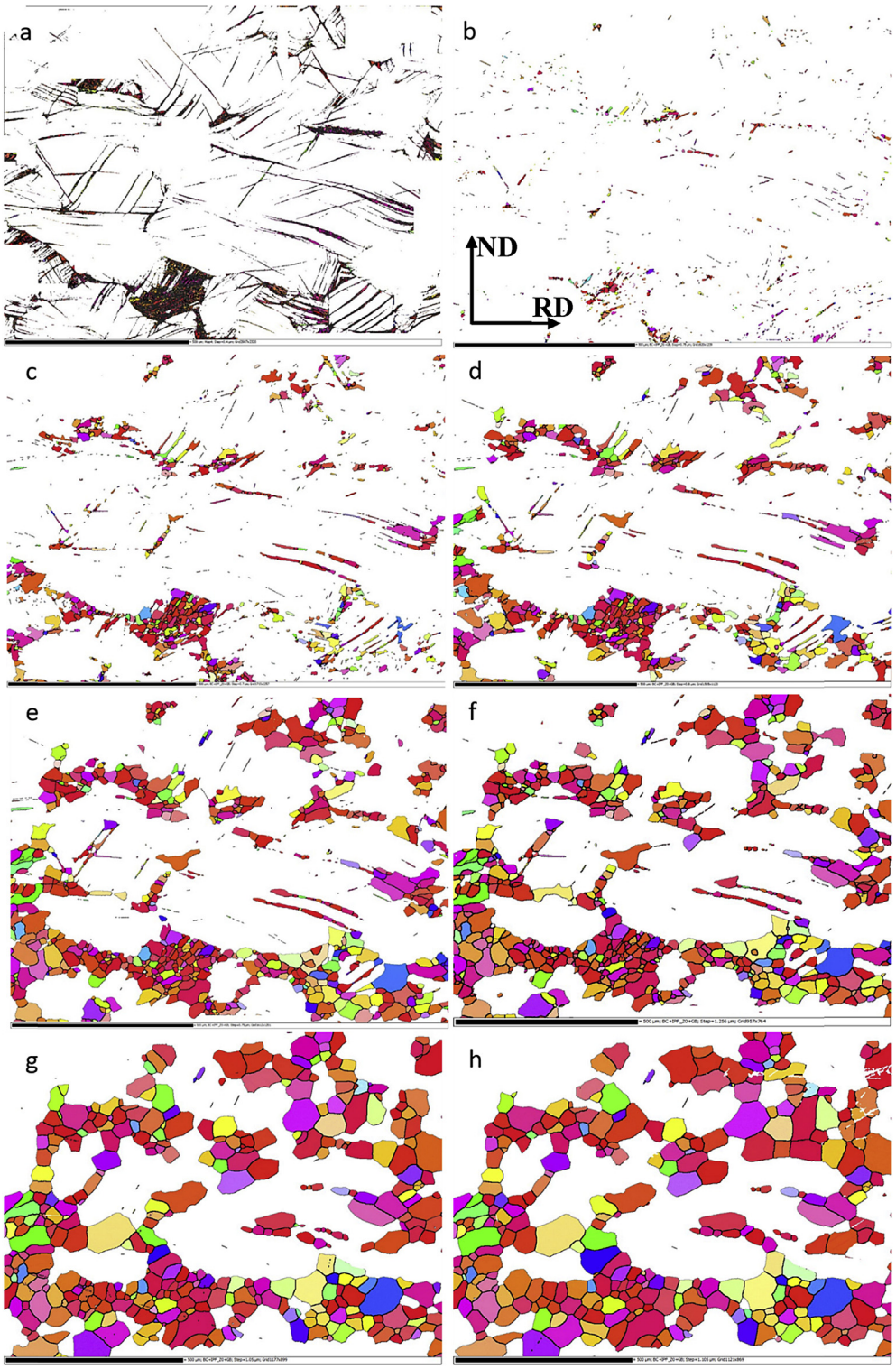

Fig. 5. EBSD IPF subset maps showing Rex-grains induced by DTW and DTW-GB intersections at annealing intervals of (a) 0, (b) 11, (c) 18, (d) 28, (e) 58, (f) 98, (g) 198 and (h) 378 min. Scale bar: 500 μm. The axes systems are all the same as shown in Fig. 5(b).

the sample was protected. To remove any oxide from the surface of interest for next EBSD scan, the annealed sample was given a mild polish using 40 nm OPS suspension. The thickness reduction after this mild polishing was less than 1 μm, measured by a micrometer.

3. Results

3.1. As-deformed microstructure

Fig. 1(a) shows the as-received sample microstructure. Intermetallic compounds were located along grain boundaries. Fig. 1(b)

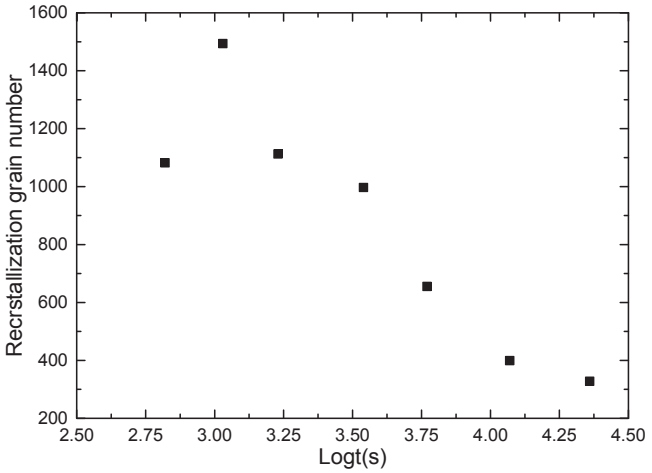

Fig. 6. Numbers of recrystallized grains originating from DTWs and DTW-GB intersections as function of annealing time.

shows an EBSD Inverse Pole Figure (IPF) map from which average grain size was found to be 16.5 μm. In order to dissolve the second particles into the matrix and produce a wide grain size distribution (since the grain size has a significant effect on the twin modes [22,27,36,37]), the as-received material was solid solution treated at 525 °C for 24 h (SST24). Nevertheless, some sparsely distributed Y enriched particles were still observed and will be presented in the following sections. Fig. 1(c) and (d) give an EBSD IPF map of the SST24 and grain size distribution histograms. The solution heat treatment resulted in a grain size in the range of 20–450 μm, which produced a variety of different twin types and twin mixtures after cold rolling, allowing the effect of each deformation twin type to be investigated in one specimen.

Fig. 2(a) shows an IPF map of a SST24 sample subjected to 20% thickness reduction in one pass. The pole figure as shown in Fig. 2(b) appears to show intense preferred orientation, but this was due to the presence of a large grain (purple colour in the IPF map) and the limited number of sampled grains. Deformation twins can clearly be seen in all grains (Fig. 2(c)), with Fig. 2(e) giving the main twin type and variants produced in this specimen. The dominant twin boundaries are TTW, TTW-TTW and DTW. The amount of CTW boundaries are limited due to the rapid transformation of CTW to DTW fragments by secondary $\{10\bar{1}2\}$ twinning [38]. The commonly

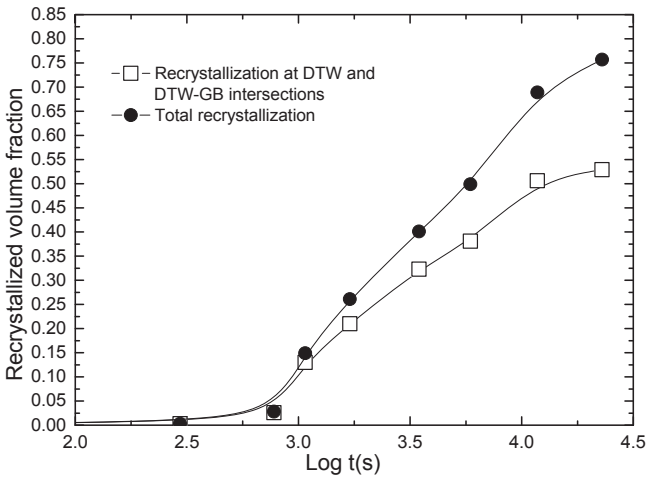

Fig. 7. Recrystallized volume fraction as function of annealing time.

reported twin types and twin variants produced in Mg alloys are summarized in Tables 2 and 3 [35,38].

3.2. Mechanisms of twin evolution

Seven deformed grains containing mainly TTW, DTW network, DTW lamellae, networks between DTWs and different TTW variants, and DTW-GB intersections. All the twin boundary misorientations were determined, Tables 2 and 3 and Fig. S1 (Fig. S1 in Supplementary file).

Fig. 3(a–e) gives the evolution of the TTWs during static annealing. During the whole process, no recrystallization occurred within the TTWs, which is consistent with published work [12]. Recrystallization, such as the recrystallized grains labelled as 1–8 in Fig. 3(b,d), initiated along locally heavy strained GB segments after annealing for 18 min. The recrystallized grain 9 was stimulated by a Y enriched particle (see Fig. S2). With further annealing, these recrystallized grains grew into the deformed parent grain and the TTWs. Although there are several intersections between TTWs, no recrystallization took place around these sites. Some residual TTW segments can be seen in grain 4 (Fig. 3(d)). When annealed for 58 min, recrystallization occurred by subgrain boundary migration (grains 10,11 in Fig. 3(d) which subsequently consumed the adjacent deformed grain with further annealing.

Fig. 3(f–k) shows a deformed grain containing primary TTWs and secondary DTWs formed in a primary TTW, defined as a tertiary twin. Also, two sets of undefined 30°–38°$\langle 0\bar{1}10\rangle$ twins (white arrows shown in Fig. 3(f)) were observed. This type of twin could be originally from 38°$\langle 11\bar{2}0\rangle$ $\{10\bar{1}1\}$-$\{10\bar{1}2\}$ double twins that was subsequently subjected to extensive prismatic slip. This slip would have rotated the twinned volume by 30° around the c-axis of the twin and resulted in the observed 38°$\langle 10\bar{1}0\rangle$ orientation relationship with matrix [18]. The identification of each twin type is presented in Fig. S3. After 18 min annealing, recrystallized grains nucleated and grew rapidly in non-indexed heavy local strain areas, such as triple points, twin-GB intersections (from neighbour deformed grain), and heavy strained GB segments mentioned above. Furthermore, recrystallized grains labelled 1–3 (Fig. 3(h)) within an undefined twin grew beyond twin boundaries until they met other recrystallized grains (Fig. 3(k)). Even at the intersection of two large TTWs, no recrystallization occurred.

Fig. 3(l) shows a DTW network. Once recrystallization had initiated, recrystallized grains readily grew towards non-indexed areas with higher internal stored energy after annealing for 18 min. After 58 min annealing, the deformed grain was almost completely recrystallized. After 198 min, the recrystallized grains formed at the DTW network had consumed the whole parent grain except grain 1 in Fig. 3(q). recrystallized grains 2 and 3 had even expanded into the neighbouring deformed grains.

Fig. 4(a–g) shows three adjacent deformed grains consisting of mainly DTWs. The right grain only contained parallel DTWs arrays, while the left and upper ones contained intersected DTWs. Although single lamellae recrystallized only after 11 min annealing, the recrystallized grains were confined by the twin boundaries. These recrystallized grains within the DTW were consumed by the adjacent larger recrystallized grains later on, so their contribution to the final texture modification was very limited, if at all. A separated DTW (arrowed in black) in Fig. 3(m) was also replaced with further annealing. In contrast, little recrystallization had occurred in the left and upper deformed grains after 11 min annealing, but recrystallization was subsequently rapid and propagated to consume the whole region.

Fig. 4(h–n) presents a deformed grain containing TTW variant $\{10\bar{1}2\}$-$\{\bar{1}012\}$ and DTW (Fig. 2(c) and Fig. S1(e)). The recrystallization nucleation site and grain growth were quite similar to TTW

and DTW evolution described above. Similarly, in Fig. 4(o–t), the same recrystallization process occurred: only locally high strain area caused by DTWs recrystallize and these recrystallized grains favourably extended into the parent grain and TTWs. Even though TTWs and TTW variant $\{10\bar{1}2\}$-$\{\bar{1}012\}$ intersect with each other, no extra locally higher strain was introduced either within twins or around junction points.

Fig. 4(u-za) shows the evolution process of DTW twin-twin and DTW-GB intersections. Recrystallization began at these intersections after 11 min annealing. These grains preferentially grew towards the DTW. After 28 min, recrystallized grains 1–4 in Fig. 4(y) originating from either narrowly distributed DTW or DTW twin-twin intersections appeared and quickly consumed the entire deformed grain area.

3.3. Recrystallization volume fraction contributed by twins

Because no recrystallization occurred in TTWs or TTW twin variants, recrystallization only originating from DTWs and DTW-GB intersections were statistically analysed to understand their contribution to the final crystallographic texture modification. Fig. 5(a) shows a subset map of the as-deformed sample containing only DTWs and some GB segments attaching to the ends of the DTWs. The volume fraction is ~11%. Fig. 5(b–h) gives the evolution of recrystallized grains originating from DTWs and DTW-GB intersections after 11, 18, 28, 58, 981 198 and 378 min. These maps allowed us to exactly locate the origin of the recrystallized grains as well as follow their growth. Fig. 5(b) shows all the recrystallized grains after 11 min annealing where the recrystallized volume fraction was only 2.6%. The low volume fraction at this stage could be attributed to a long incubation time. The recrystallized volume fraction increased quickly to 13% and 21% after 18 and 28 min annealing. With further annealing, only grain growth of existing recrystallized grains occurred, Fig. 5(e–h), for example, compare Fig. 5(d)–(c). This is shown further in Fig. 6 which gives the number of recrystallized grains from the DTWs and DTW-GB intersections only throughout the whole annealing process. The recrystallized grain numbers reached the peak after 18 min annealing and decreased thereafter for longer annealing times showing that grain growth was the dominant process.

Fig. 7 plots the total recrystallization volume fraction (V_t) and recrystallization only in DTWs and DTW-GB intersections (V_{dtw}) as a function of annealing time. It shows nearly all recrystallized grains were from DTWs and DTW-GB intersections even after annealing for 18 min. Subsequently, recrystallized grains from other recrystallization sites started to exhibit extensive recrystallization and grain growth. However, the rate of recrystallization was not comparable to the recrystallized grains formed by DTWs and DTW-GB intersections until after annealing for 198 min. After 378 min annealing, V_t was ~75.7%, while V_{dtw} is up to ~52.9%, which represents ~69.9% of V_t.

Fig. 8 shows (0002) pole figures of recrystallized grains formed only in DTWs and DTW-GB intersections during the whole annealing process. Regardless of the annealing time, the recrystallized texture components were off-basal and totally different from the as-deformed texture (Fig. 1(b)). The most significant changes during the whole annealing processes were the weakening of texture component A (TCA), enhancement of texture component B (TCB) and texture component C (TCC) (as marked in Fig. 8). To find out the detailed texture evolution, the grains that contributed to the three texture components were located and compared. Fig. 9 shows 3 sets of EBSD subsets used to track the texture components evolutions. After annealing for 11 min, Fig. 9(a) shows that recrystallized grains within parallel DTWs lamellae were the main source for the formation of TCA. With further annealing for 18 min, most of these narrow grains were replaced by adjacent recrystallized grains (Fig. 9(b)). The TCB component became obvious after annealing for 18 min (Fig. 9(c)), and it was enhanced with further annealing (Fig. 9(d)). As shown in Fig. 9(e and f), the enhancement of TCC can be attributed to the recrystallized grains growth during annealing.

4. Discussion

There were common features to the recrystallization mechanisms in the different twin types. Firstly, only twin or twin variants inducing high local strain acted as effective nucleation sites for recrystallization. Secondly, whether the recrystallized grains can grow out of original twin boundaries depends strongly on the stored energy in adjacent areas.

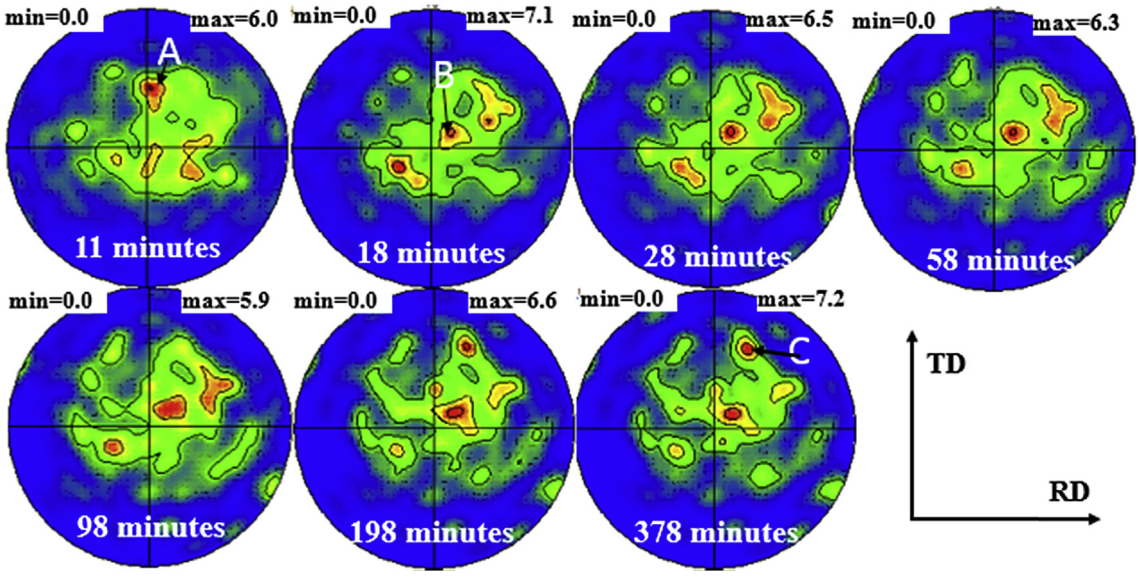

Fig. 8. (0002) pole figures consisting only of recrystallized grains formed at DTWs and DTW-GB intersections.

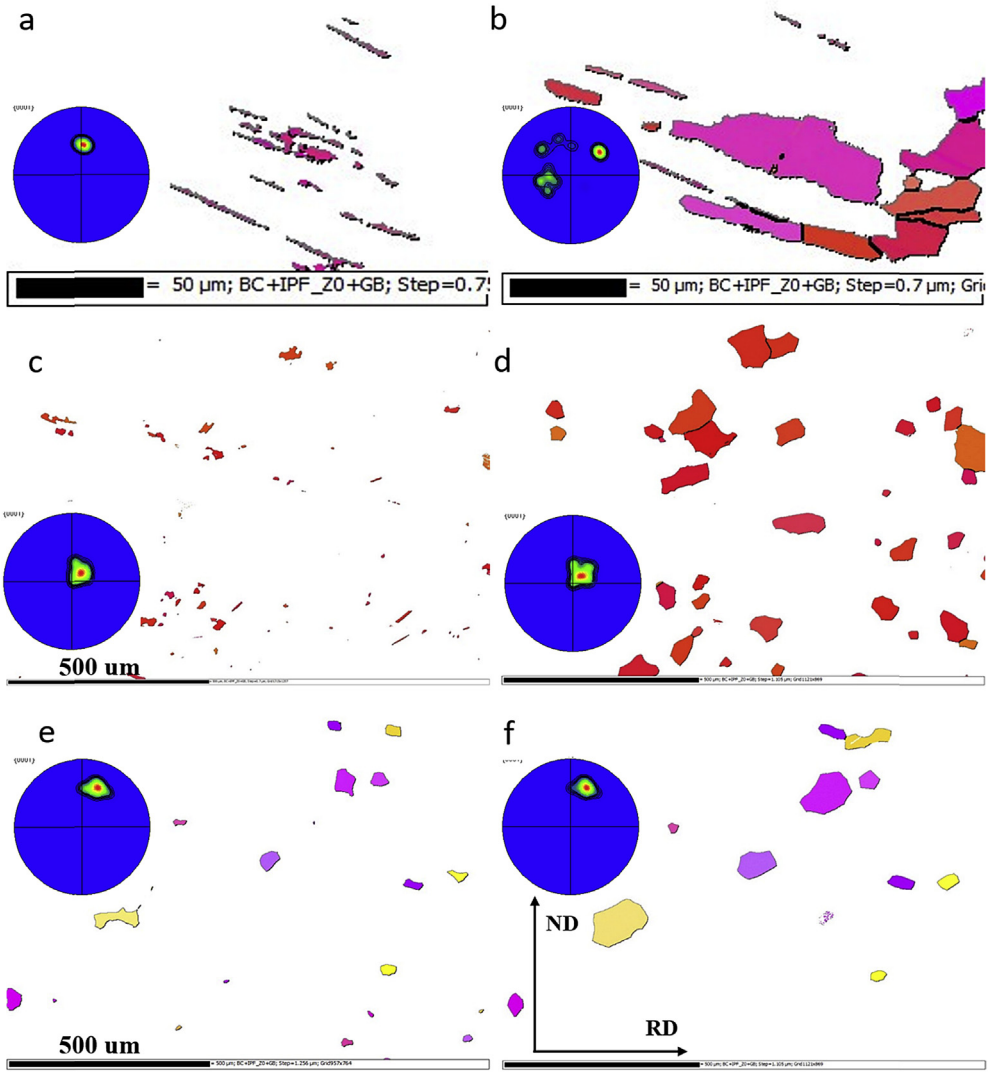

Fig. 9. EBSD IPF subset maps showing recrystallized grains from (a) texture component A (Fig. 8) after 11 min annealing and (b) 18 min annealing; (c) texture component B after 18 min annealing and (d) 378 min annealing; (e) texture component c after 98 min annealing and (f) 378 min annealing. All the insets are corresponding (0002) pole figures. The axes systems are all the same as shown in Fig. 9(f).

Fig. 2(f) shows a Schmid Factor map of the EBSD area. Because the stored energy required for recrystallization cannot be accumulated without sufficient basal slip [15], it is not surprising that it is rare to see recrystallization occurring within TTWs oriented with low Schmid Factors for basal slip (e.g. grain A in Figs. 1(f) and 3(a–e)). TTW and TTW variants with high Schmid Factor for basal slip (e.g. grains B and C in Fig. 1(f)) were also easily observed. Fig. 10 provides the Schmid Factor map of these three grains, which mainly contained tension twins. For grain A, the average Schmid Factor within TTWs was ~0.24. Therefore, no recrystallization occurred within these TTWs, as expected. In contrast, the average Schmid Factor for grains B and C was ~0.42, but there was no recrystallization within these TTWs, rather, these TTWs were consumed by the adjacent recrystallized grains (Fig. 5(h–t)). This can be attributed to the following two reasons. Firstly, the critical resolved shear stress (CRSS) required for the formation of TTWs is relatively low, while CTWs and DTWs require high stresses to form. Therefore, the amount of elastic strain energy that is released during annealing is much greater in the case of CTWs and DTWs than in TTWs [22]. Secondly, the interaction between twin boundaries and dislocations could also play a key role in accumulation of dislocations along twin boundaries. Kadiri et al. [23] used molecular dynamics simulations to investigate why TTWs are profuse in Mg. They reported TTWs are efficient sinks for basal dislocations, which can fully absorb the lattice dislocations near tension twin boundaries and make TTWs grow easily. This can negate the twin shear localization to some extent. In addition, Molodov et al. [39] found basal slip can readily transmit through TTWs twinning boundaries, which could effectively relieve the local stress and dislocation pile-ups along TTWs twin boundaries. Therefore, no matter what the crystal orientation of the TTW with respect to the applied stress axis, basal dislocations were not accumulated. Therefore, there was inadequate elastic strain energy to activate recrystallization within a TTW. Consequently, no recrystallization occurred during annealing within TTWs.

Due to easy basal slip within twins and the accumulation of dislocations around twin boundaries, recrystallization was often observed within CTWs and DTWs [9,12,18,28,31]. Almost all DTWs acted as nucleation sites for initial recrystallization due to high local strain, believed to be caused by intense basal slip within DTWs. To confirm this, we performed In-grain Misorientation Axis (IGMA) analysis to determine the slip mode within DTWs. Fig. 11(a) and (c)

show intersected DTWs and parallel DTW segments, and Fig. 11(b) and (d) present the corresponding IGMA distributions. The results indicate the rotation axis in these two DTW areas is $\langle\bar{1}2\bar{1}0\rangle$. This distribution is caused by basal slip within DTWs according to Chun and Davies [38,40].

During subsequent grain growth, the recrystallization grains extend quickly towards higher stored energy areas. For parallel DTW arrays, recrystallized grains within DTWs can only extend along the interior of the twin as the twin boundaries act as strong barriers to growth, resulting in bands of recrystallized grains. However, these bands of recrystallized grains within DTWs did not contribute to the final texture since they were consumed by the growth of separate larger recrystallized during further annealing, (Fig. 4(a–g)). In contrast, where a DTW end meets a heavily strained grain boundary segment, the intersection point usually has higher stored energy and is not fully constrained by twin boundaries. Fig. 12(a) shows a kernel average misorientation (KAM) map of Fig. 4(u). The black areas have the greatest lattice

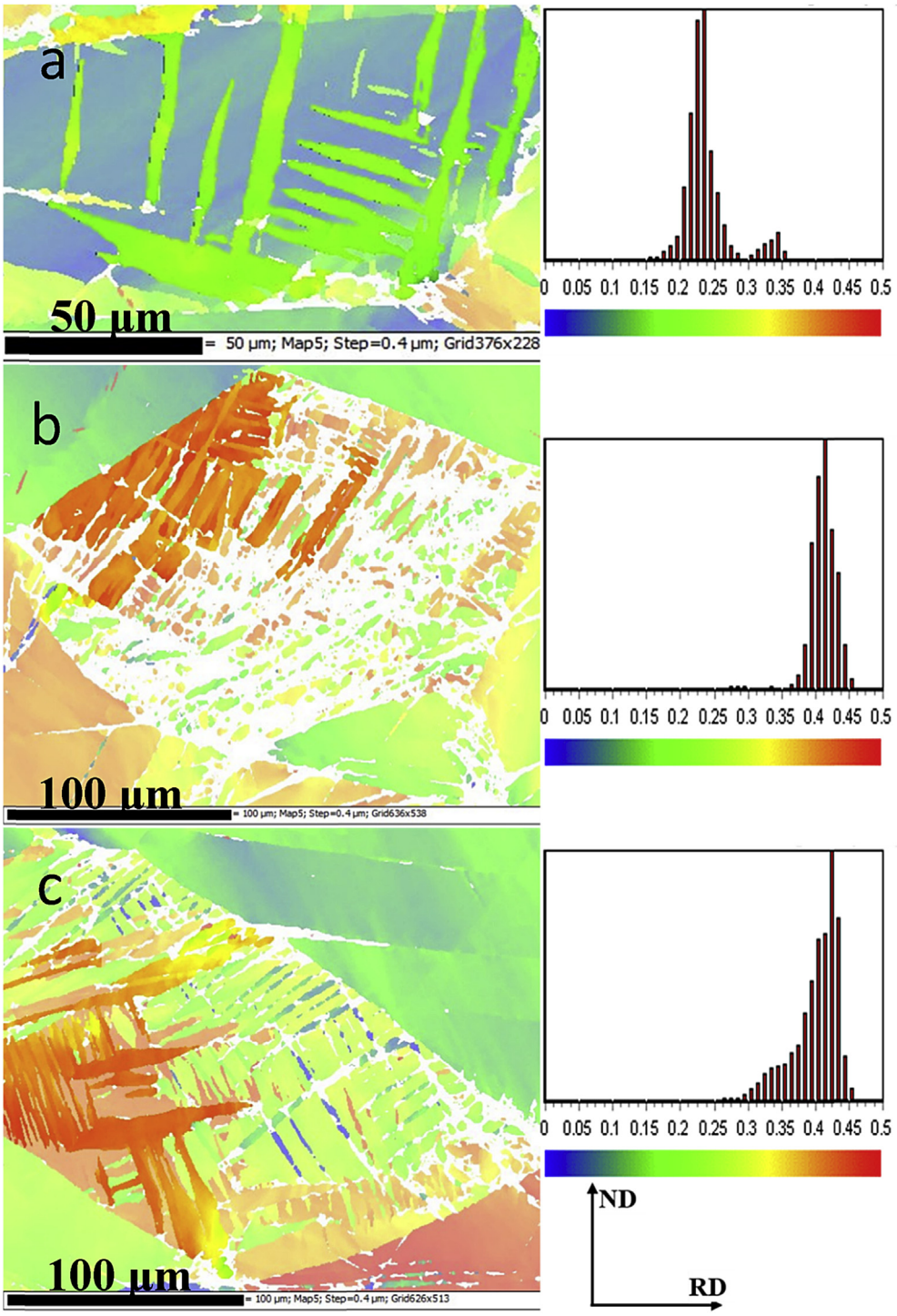

Fig. 10. Basal Schmid factors maps and distribution functions in (a) TTW, (b) TTW-TTW variant and DTW, and (c) TTW, TTW-TTW variant and DTW containing grains. The axes systems are all the same as shown in Fig. 10(c).

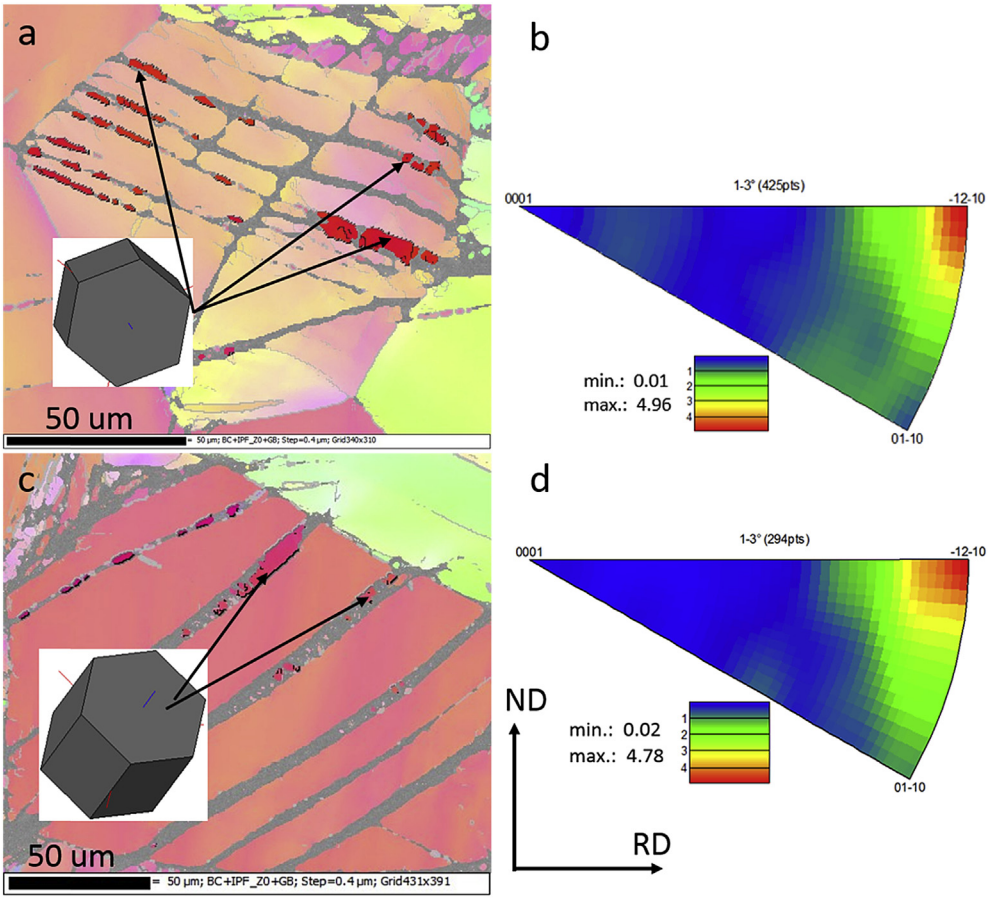

Fig. 11. IGMA distributions of the DTWs containing grains: (a–b) DTW network, and (c–d) single arrays of lamellae. The inset 3D crystal orientation coordinate system relates to the primary sample axes (CS_0).

distortion and thus have higher local misorientation than those areas that have been indexed. The growth direction is dependent on the distribution of internal stored energy (higher KAM values). It is obvious that the growth direction followed the local strain distribution. These recrystallized grains grew quickly along the DTWs or consumed deformed parent grain area with higher stored energy (Fig. 4(u–y)). Fig. 12(b) also gives a KAM map of Fig. 3(l). At the intersections between DTWs, the recrystallized grains could easily grow into the deformed grain because of the local dislocation pile-ups and lack of intact twin boundaries. These recrystallized grains not only consumed deformed parent grains but also expanded into neighbouring deformed grains because of the high residual stored energy in the adjacent grains (Fig. 3(l–q)).

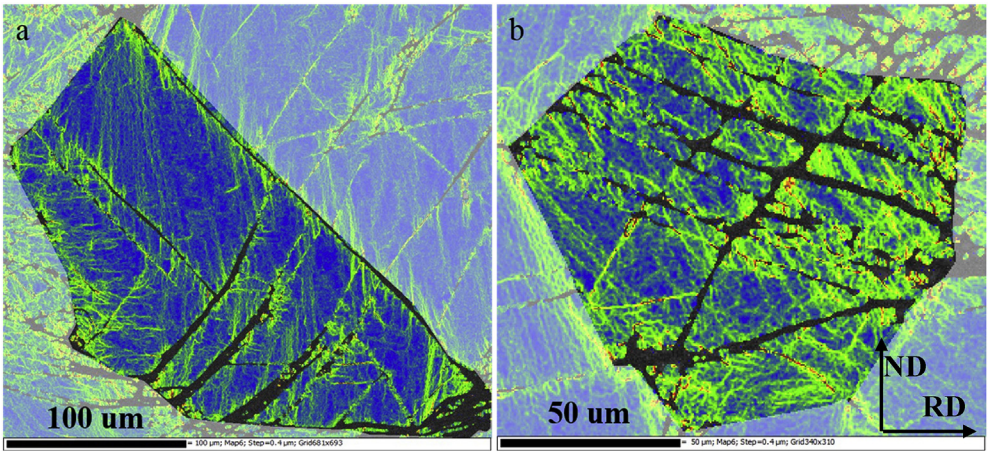

Fig. 12. KAM maps of (a) heavily strained twin-GB and (b) DTW network containing deformed grains showing the stored energy distribution (for indexed areas, the higher degree of misorientation is seen in the brighter green colour. The non-indexed areas have the highest local strain). The axes systems are all the same as shown in Fig. 12(b). (For interpretation of the references to colour in this figure legend, the reader is referred to the web version of this article.)

As shown in Fig. 7, V_{dtw} is nearly equal to V_t after annealing for 18 min. High local strain caused by intensive basal slip in soft orientation DTWs results in DTWs becoming preferential sites for nucleation and growth of recrystallization. This effect is further enhanced around the intersections between DTWs. During further annealing, new recrystallized grains had no growth advantage when they met already existed larger recrystallized grains originating from DTW-DTW or DTW-GB intersections. Therefore, the recrystallized volume fraction from double twins (V_{dtw}) should increase during subsequent annealing, and indeed this is shown in Fig. 7. Recrystallized grains originating from twin nucleation sites have random orientations [13]. Therefore, texture modification during annealing shown in Fig. 8 can be attributed to the combined effects of preferential nucleation site, random orientated recrystallized grains, and high stored energy around DTWs and DTW-GB intersections required for grain growth.

As a result of concerns around flow localization and crack formation due to DTWs [26], research has focused on decreasing or eliminating CTWs or DTWs by alloying or grain refinement methods [26,37,40,41]. However, the flow localization introduced by DTWs is critical for recrystallization at twin sites, since recrystallization does not occur in TTWs and TTW variants. If DTWs are eliminated from the microstructure, there would be no twin recrystallization. Furthermore, flow localization as a result of small CTWs or DTWs triggers the formation of shear bands [26,41,42]. In dilute or fully solid solution treated Mg alloys, there is no particle stimulated recrystallization either. Only grain boundary nucleation would be available if CTWs and DTWs are suppressed. Grain boundary nucleation does not lead to significant texture modification from the deformed basal texture. Therefore, if CTWs or DTWs are restricted during deformation in Mg alloys without second phase particles, it will be difficult to weaken the basal texture. Lentz et al. [27] argued it is not DTWs themselves, but the absence of plastic relaxation mechanisms that results in failure. They reported that the plastic strain can be relieved by activation of c+a⟩ pyramidal slip in a Mg-4wt%Li with copious DTWs, leading to a high compressive failure strain of 33%. They also provided evidence that the onset of DTW cannot trigger immediate cracking. Therefore, this side effect can be eliminated, and more related work needs to carry out to minimize the voids or cracks in the vicinity of DTWs. Only in this way can we produce Mg alloys with weakened texture and good mechanical properties.

5. Conclusions

In summary, the recrystallization process during static annealing were accurately tracked by using a *quasi-in-situ* EBSD method in this work. The initial formation of recrystallization grains, the subsequent growth and/or replacement was followed in a site specific manner. The evolution of DTWs recrystallization texture was monitored for the first time during the entire static annealing process. This has allowed the precise identification of the recrystallization mechanisms as a function of twin types, twin variants, and twin-twin and twin-grain boundary intersections. The following conclusions can be proposed:

(1) All the tension twins and tension twin variants did not recrystallize during the whole annealing process and were consumed by the adjacent recrystallized grains during the grain growth stage, due to minimal accumulation of dislocations and consequentlty low elastic strain energy along twin boundaries.
(2) The preferential nucleation site for recrystallization observed in this work was $\{10\bar{1}1\}$-$\{10\bar{1}2\}$ double twins (DTWs). Nearly all recrystallized grains were from DTWs and DTW-GB intersections even after annealing for 18 min and all DTWs recrystallized during the early stage of annealing. However, during subsequent growth, the recrystallized grains within the individual DTW lamellae were constrained and consumed by the other recrystallized grains in the end. Thus, their contribution to the recrystallized texture was eliminated. In contrast, recrystallizating grains originating from DTW-DTW and DTW-GB intersections readily grew into the deformed parent grains and subsequently even into neighbouring deformed grains, extending quickly into regions of higher stored energy.
(3) Recrystallized grains originating from DTW-DTW and DTW-GB intersections grew towards the deformed grains through the whole annealing process. After 378 min annealing, V_t was ~75.7% while the volume fraction arising from double twins V_{dtw} was ~52.9%. Hence, the V_{dtw} accounts for ~69.9% of the V_t. This is a high proportion of the total recrystallized fraction, which suggests that the contribution of recrystallization from double twins has been completely underestimated in the past. In addition, recrystallization from DTW-DTW and DTW-GB intersections exhibited a weak, non-basal texture.
(4) Given that this was the dominant type of recrystallization that consumed the deformed microstructure, this form of twinning is particularly important in producing an alloy with weak, non-basal texture. Thus, a full understanding of the twin formation, subsequent recrystallization mechanisms and corresponding contribution to texture modification provides new insight into designing new wrought Mg alloys and optimizing thermomechanical processes to improve formability of commercial Mg alloys.

Acknowledgements

This work was funded by the EPSRC DARE Project, EP/L025213/1.

Appendix ASupplementary data

Supplementary data related to this article can be found at http://dx.doi.org/10.1016/j.actamat.2016.12.058.

References

[1] E.A. Ball, P.B. Prangnell, Tensile-compressive yield asymmetries in high strength wrought magnesium alloys, Scr. Metall. Mater. 31 (1994) 111–116.
[2] N. Stanford, D. Atwell, A. Beer, C. Davies, M.R. Barnett, Effect of microalloying with rare-earth elements on the texture of extruded magnesium-based alloys, Scr. Mater. 59 (2008) 772–775.
[3] T. Al-Samman, X. Li, Sheet texture modification in magnesium-based alloys by selective rare earth alloying, Mater. Sci. Eng. A 528 (2011) 3809–3822.
[4] J. Bohlen, M.R. Nürnberg, J.W. Senn, D. Letzig, S.R. Agnew, The texture and anisotropy of magnesium–zinc–rare earth alloy sheets, Acta Mater. 55 (2007) 2101–2112.
[5] D. Griffiths, Explaining texture weakening and improved formability in magnesium rare earth alloys, Mater. Sci. Technol. 31 (2015) 10–24.
[6] Z.R. Zeng, Y.M. Zhu, S.W. Xu, M.Z. Bian, C.H.J. Davies, N. Birbilis, J.F. Nie, Texture evolution during static recrystallization of cold-rolled magnesium alloys, Acta Mater. 105 (2016) 479–494.
[7] S.R. Agnew, J.F. Nie, Preface to the viewpoint set on: the current state of magnesium alloy science and technology, Scr. Mater. 63 (2010) 671–673.
[8] B.-C. Suh, M.-S. Shim, K.S. Shin, N.J. Kim, Current issues in magnesium sheet alloys: where do we go from here? Scr. Mater. 84–85 (2014) 1–6.
[9] J. Hirsch, T. Al-Samman, Superior light metals by texture engineering: optimized aluminum and magnesium alloys for automotive applications, Acta Mater. 61 (2013) 818–843.
[10] F.J. Humphreys, M. Hatherly, Recrystallization and Related Annealing Phenomena, Elsevier Science, 2004.
[11] C. Drouven, I. Basu, T. Al-Samman, S. Korte-Kerzel, Twinning effects in deformed and annealed magnesium–neodymium alloys, Mater. Sci. Eng. A 647 (2015) 91–104.
[12] I. Basu, T. Al-Samman, Twin recrystallization mechanisms in magnesium-rare earth alloys, Acta Mater 96 (2015) 111–132.
[13] É. Martin, R.K. Mishra, J.J. Jonas, Effect of twinning on recrystallisation textures

in deformed magnesium alloy AZ31, Philos. Mag. 91 (2011) 3613–3626.
[14] N. Stanford, M.R. Barnett, The origin of “rare earth” texture development in extruded Mg-based alloys and its effect on tensile ductility, Mater. Sci. Eng. A 496 (2008) 399–408.
[15] Q. Ma, B. Li, W.R. Whittington, A.L. Oppedal, P.T. Wang, M.F. Horstemeyer, Texture evolution during dynamic recrystallization in a magnesium alloy at 450 °C, Acta Mater. 67 (2014) 102–115.
[16] J.J. Bhattacharyya, S.R. Agnew, G. Muralidharan, Texture enhancement during grain growth of magnesium alloy AZ31B, Acta Mater. 86 (2015) 80–94.
[17] M.A. Steiner, J.J. Bhattacharyya, S.R. Agnew, The origin and enhancement of texture during heat treatment of rolled AZ31B magnesium alloys, Acta Mater. 95 (2015) 443–455.
[18] K.D. Molodov, T. Al-Samman, D.A. Molodov, G. Gottstein, Mechanisms of exceptional ductility of magnesium single crystal during deformation at room temperature: multiple twinning and dynamic recrystallization, Acta Mater. 76 (2014) 314–330.
[19] B.-C. Suh, J.H. Kim, J.H. Hwang, M.-S. Shim, N.J. Kim, Twinning-mediated formability in Mg alloys, Sci. Rep. 6 (2016) 22364.
[20] H.E. Friedrich, B.L. Mordike, Magnesium Technology: Metallurgy, Design Data, Applications, Springer, New York, 2010.
[21] I.J. Polmear, Light Alloys: from Traditional Alloys to Nanocrystals, Elsevier/Butterworth-Heinemann, 2006.
[22] B.C. Wonsiewicz, Plasticity of Magnesium Crystals (Ph.D. thesis), Massachusetts Institute of Technology, 1966.
[23] H. El Kadiri, C.D. Barrett, J. Wang, C.N. Tomé, Why are twins profuse in magnesium? Acta Mater. 85 (2015) 354–361.
[24] S. Mu, J.J. Jonas, G. Gottstein, Variant selection of primary, secondary and tertiary twins in a deformed Mg alloy, Acta Mater. 60 (2012) 2043–2053.
[25] M.R. Barnett, Twinning and the ductility of magnesium alloys: Part I: “Tension” twins, Mater. Sci. Eng. A 464 (2007) 1–7.
[26] M.R. Barnett, Twinning and the ductility of magnesium alloys: Part II. “Contraction” twins, Mater. Sci. Eng. A 464 (2007) 8–16.
[27] M. Lentz, M. Risse, N. Schaefer, W. Reimers, I.J. Beyerlein, Strength and ductility with $\{10\bar{1}1\}$ — $\{10\bar{1}2\}$ double twinning in a magnesium alloy, Nat. Commun. 7 (2016).
[28] X. Li, P. Yang, L.N. Wang, L. Meng, F. Cui, Orientational analysis of static recrystallization at compression twins in a magnesium alloy AZ31, Mater. Sci. Eng. A 517 (2009) 160–169.
[29] T. Al-Samman, K.D. Molodov, D.A. Molodov, G. Gottstein, S. Suwas, Softening and dynamic recrystallization in magnesium single crystals during c-axis compression, Acta Mater. 60 (2012) 537–545.
[30] A. Jäger, P. Lukáč, V. Gärtnerová, J. Haloda, M. Dopita, Influence of annealing on the microstructure of commercial Mg alloy AZ31 after mechanical forming, Mater. Sci. Eng. A 432 (2006) 20–25.
[31] M.H. Yoo, Slip, twinning, and fracture in hexagonal close-packed metals, Metall. Trans. A 12 (1981) 409–418.
[32] A. Levinson, R.K. Mishra, R.D. Doherty, S.R. Kalidindi, Influence of deformation twinning on static annealing of AZ31 Mg alloy, Acta Mater. 61 (2013) 5966–5978.
[33] T. Al-Samman, G. Gottstein, Dynamic recrystallization during high temperature deformation of magnesium, Mater. Sci. Eng. A 490 (2008) 411–420.
[34] M. Sanjari, A. Farzadfar, A.S.H. Kabir, H. Utsunomiya, I.-H. Jung, R. Petrov, L. Kestens, S. Yue, Promotion of texture weakening in magnesium by alloying and thermomechanical processing: (I) alloying, J. Mater. Sci. 49 (2014) 1408–1425.
[35] M.D. Nave, M.R. Barnett, Microstructures and textures of pure magnesium deformed in plane-strain compression, Scr. Mater. 51 (2004) 881–885.
[36] P. Dobroň, F. Chmelík, S. Yi, K. Parfenenko, D. Letzig, J. Bohlen, Grain size effects on deformation twinning in an extruded magnesium alloy tested in compression, Scr. Mater. 65 (2011) 424–427.
[37] M. Lentz, A. Behringer, C. Fahrenson, I.J. Beyerlein, W. Reimers, Grain size effects on primary, secondary, and tertiary twin development in Mg-4 wt pct Li (-1 wt pct Al) alloys, Metall. Mater. Trans. A 45 (2014) 4737–4741.
[38] S. Niknejad, S. Esmaeili, N.Y. Zhou, The role of double twinning on transgranular fracture in magnesium AZ61 in a localized stress field, Acta Mater. 102 (2016) 1–16.
[39] K.D. Molodov, T. Al-Samman, D.A. Molodov, Profuse slip transmission across twin boundaries in magnesium, Acta Mater. 124 (2017) 397–409.
[40] M.R. Barnett, S. Jacob, B.F. Gerard, J.G. Mullins, Necking and failure at low strains in a coarse-grained wrought Mg alloy, Scr. Mater. 59 (2008) 1035–1038.
[41] A. Jain, O. Duygulu, D.W. Brown, C.N. Tomé, S.R. Agnew, Grain size effects on the tensile properties and deformation mechanisms of a magnesium alloy, AZ31B, sheet, Mater. Sci. Eng. A 486 (2008) 545–555.
[42] S. Sandlöbes, S. Zaefferer, I. Schestakow, S. Yi, R. Gonzalez-Martinez, On the role of non-basal deformation mechanisms for the ductility of Mg and Mg–Y alloys, Acta Mater. 59 (2011) 429–439.